

Article

On the Stability and Electronic Structure of Transition-Metal Dichalcogenide Monolayer Alloys $\text{Mo}_{1-x}\text{X}_x\text{S}_{2-y}\text{Se}_y$ with $\text{X} = \text{W}, \text{Nb}$

Agnieszka Kuc^{1,*†} and Thomas Heine^{1,2,†}

Received: 2 November 2015; Accepted: 15 December 2015; Published: 30 December 2015

Academic Editor: Frank Schwierz

¹ Wilhelm-Ostwald-Institut für Physikalische und Theoretische Chemie, Universität Leipzig, Linnéstr. 2, 04103 Leipzig, Germany; thomas.heine@uni-leipzig.de

² Department of Physics and Earth Sciences, Jacobs University Bremen, Campus Ring 1, 28759 Bremen, Germany

* Correspondence: agnieszka_beata.kuc@uni-leipzig.de; Tel.: +49-341-97-36405; Fax: +49-341-97-36399

† These authors contributed equally to this work.

Abstract: Layered transition-metal dichalcogenides have extraordinary electronic properties, which can be easily modified by various means. Here, we have investigated how the stability and electronic structure of MoS_2 monolayers is influenced by alloying, *i.e.*, by substitution of the transition metal Mo by W and Nb and of the chalcogen S by Se. While W and Se incorporate into the MoS_2 matrix homogeneously, forming solid solutions, the incorporation of Nb is energetically unstable and results in phase separation. However, all three alloying atoms change the electronic band structure significantly. For example, a very small concentration of Nb atoms introduces localized metallic states, while $\text{Mo}_{1-x}\text{W}_x\text{S}_2$ and $\text{MoS}_{2-y}\text{Se}_y$ alloys exhibit spin-splitting of the valence band of strength that is in between that of the pure materials. Moreover, small, but evident spin-splitting is introduced in the conduction band due to the symmetry breaking. Therefore, transition-metal dichalcogenide alloys are interesting candidates for optoelectronic and spintronic applications.

Keywords: transition-metal dichalcogenide monolayers; alloys; electronic structure; spin-orbit coupling; density of states; density-functional theory

1. Introduction

The electronic structure of two-dimensional (2D) layered materials, in particular transition-metal chalcogenides (TMCs), have gained enormous interest in the past five years. Special attention is paid to semiconducting TMCs of the $2H \text{TX}_2$ type (T, transition metal; X, chalcogen atom), because their electronic properties can be easily tuned by various factors, such as quantum confinement, external electric field, strain modulations or doping [1–11]. Easy tuning of the electronic structure is very important for several applications, *e.g.*, for spin- and opto-electronics.

The interest in spintronic applications of TMCs arises from the hexagonal symmetry and the finite band gap, which, depending on the stoichiometry and number of layers, is in the range of 1–2 eV. Layered TMCs with an even number of layers (*e.g.*, bilayers) have inversion symmetry, which is explicitly broken in systems with an odd number of layers (including monolayers). Hexagonal symmetry of TMCs imposes the existence of inequivalent energy valleys in the Brillouin zone (K and K'). Due to lack of inversion symmetry in monolayers, a giant spin-orbit (SO) coupling (SOC) exists in the top of the valence band, ranging from about 150 meV (MoS_2) to nearly 500 meV (WTe_2) [12,13].

Quantum confinement of bulk TMCs down to the monolayer limit results in an increase of the band gap and an indirect-direct band gap transition. Although an external electric field does not

change the electronic properties of monolayers, it causes band gap closure and spin-orbit splitting in bi- and multi-layer TMCs. The monolayer band structure can, however, be modulated by tensile strain or hydrostatic pressure, leading to semiconductor-metal transition [8–11,14,15].

Results on TMC nanotubes suggest that doping small quantities of Group 13 or Group 15 atoms results in a metallic character [16]; however, Nb doping of MoS₂ tubes was found to be unfavorable energetically [17–19]. The incorporation of a dilute impurity concentration into a host material results in significant changes to the band structure, which was shown in the cases of III-V semiconductors, e.g., the As impurity in GaN leads to a significant band gap reduction, and such a GaNAs alloy can be used for green emission [20,21]. This discovery opens up a new direction in the field of light-emitting diodes. Similarly, the addition of dilute-N impurity into the GaAs material results in low threshold laser devices [22,23].

Several experimental and theoretical studies have also been published up to date on the doping and alloy formation in TMC materials [24–30]. Many of these investigations are focused on the changes of Raman modes, optical or electronic properties in the mixed systems. For example, Raman modes, especially A_{1g} and E_{2g} , are increasing and decreasing, respectively, with W concentration in MoS₂ monolayers [26–28]. There is, however, a limited literature available on the spin-orbit splitting in the electronic structure of TMC alloys.

Among various TMCs, molybdenum disulfide (MoS₂) is the most widely-studied material. TMCs of the 2H TX₂ type are composed of two-dimensional X–T–X sheets stacked on top of one another and held together via weak interlayer interactions, allowing easy exfoliation. Each sheet is trilayered with T atoms sandwiched between two chalcogen layers, as shown in Figure 1. Therefore, doping/alloying can occur both in the T and X sites.

In this paper, we have studied the complete transition of substituted MoS₂ as (i) Mo_{1–x}W_xS₂, (ii) Mo_{1–x}Nb_xS₂ and (iii) MoS_{2–x}Se_x and discuss the stability and electronic properties of these phases. Such ternary alloys are a straightforward way of tuning the electronic properties of TMC materials and might be of great interest in the fields of electronic transport, optoelectronics, as well as spintronics. We have discussed in detail the electronic band structures and projected densities of the states of MoS₂-based alloys, showing that band gaps and the spin-splitting in the valence and conduction bands can be effectively tuned, with values in between those of the pure parental materials. Moreover, a small amount of NbS₂ mixed into the MoS₂ matrix makes it metallic. We show that semiconducting WS₂ and MoSe₂ easily form solid solutions with MoS₂, while metallic NbS₂ results in a phase separation.

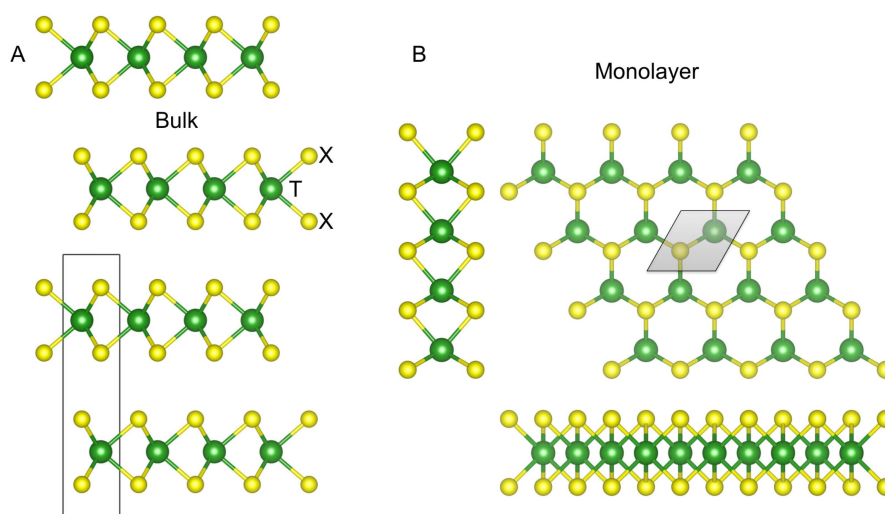


Figure 1. The atomic structure of transition-metal dichalcogenides of the 2H TX₂ type (T, transition metal; X, chalcogenide). (A) Bulk and (B) monolayer systems are shown together with their unit cells. Different sheets of TX₂ are composed of three atomic layers X–T–X, where T and X are covalently bonded. Sheets are held together by weak van der Waals forces.

2. Methods Section

In this work, we have studied atomic substitutions (alloys) in the MoS₂ monolayer. We have considered W and Nb atoms as substitutes of Mo and Se to substitute S atoms. The initial structures have hexagonal symmetry and belong to the $P6_3/mmc$ space group. The monolayers were cut out from the fully-optimized bulk structures as (0 0 1) surfaces. Alloy monolayers were further fully optimized; thus, the final symmetry is lowered. Optimization was performed using analytical energy gradients with respect to atomic coordinates and unit cell parameters within the quasi-Newton scheme combined with the BFGS (Broyden–Fletcher–Goldfarb–Shanno) scheme for Hessian updating. First-principle optimization calculations were performed on the basis of density functional theory (DFT) as implemented in the CRYSTAL09 code [31]. The exchange and correlation terms were described using general gradient approximation (GGA) in the scheme of the PBE (Perdew–Burke–Ernzerhof) [32] functional. For the sulfur and selenium atoms, the all-electron 86-311G* and 976-311d51G bases were chosen, respectively, while for heavier elements, the effective core potential (ECP) approach with large cores was employed, accounting for scalar relativistic effects [33–35]. The electronic structure calculations with the spin-orbit coupling (SOC) were performed using the PBE exchange-correlation functional and with Becke and Johnson damping (BJ-damping), as implemented in the ADF/BAND package [36,37]. Local basis functions (numerical and Slater-type basis functions of valence triple zeta quality with one polarization function (TZP)) were adopted for all atom types, and the frozen core approach (small core) was chosen.

The alloy monolayers were studied using 4×4 supercells, which consist of 16 metal atoms and 32 chalcogen atoms. The shrinking factor for bulk and layered structures was set to 8, which results in the corresponding number of 50 and 30 k -points in the irreducible Brillouin zone, respectively. The mesh of k -points for optimization calculations was obtained according to the scheme proposed by Monkhorst and Pack [38]. The SOC calculations are very time consuming and expensive; therefore, we have carried them out on smaller supercells (2×2) and alloys with 50 at% mixing. Band structures were calculated along the high symmetry points using the following path: $\Gamma - M - K - \Gamma$.

The alloying energies, E_{alloy} , were calculated as follows:

$$E_{\text{alloy}} = \frac{E_{\text{mixed}} - [x_{\text{host}}E_{\text{host}} + y_{\text{guest}}E_{\text{guest}}]}{y} \quad (1)$$

where E_{mixed} is the energy of the alloy monolayer, E_{host} is the energy of perfect MoS₂ monolayer and E_{guest} is the energy of the dopant perfect monolayer form, namely WS₂, NbS₂ and MoSe₂. x and y denote stoichiometric factors and refer to the number of formula units of each species. For example, in the case of Mo₁₂W₄S₃₂ with 6.25 at% W substitution, $x = 12$ and $y = 4$, giving:

$$E_{\text{alloy}} = \frac{E_{\text{Mo}_{12}\text{W}_4\text{S}_{32}} - [12E_{\text{MoS}_2} + 4E_{\text{WS}_2}]}{4} \quad (2)$$

E_{alloy} are given per TX₂ formula unit of the guest species (dopants).

3. Results and Discussion

We have studied three different ternary alloys on the MoS₂ monolayer with W, Nb and Se atoms. The alloying energies were calculated for all materials according to Equation (2) and given per dopant formula unit as TX₂. Band structures and the atom-projected densities of states were calculated with and without spin-orbit coupling correction. We have studied the W-MoS₂ alloy in great detail; however, general conclusions can also be drawn from the less-detailed analysis of Se- and Nb-MoS₂ alloys. The W and Se alloys with the MoS₂ monolayer are two examples of semiconductor-semiconductor alloys, while the one with Nb represents a metal-semiconductor alloy. It is important to note that dopant/alloy concentrations discussed hereafter are given as atomic percent of the metal atoms in the host material, e.g., 1 W atom in the 4×4 MoS₂ supercell (total of 16 Mo atoms) gives 6.25 at% of W.

3.1. MoS₂ Alloys with W

The MoS₂ monolayer, as well as all W-alloys were fully optimized in terms of lattice vectors and atomic positions. The optimized lattice parameters of W(Mo)-based Mo(W)S₂ alloys are given in Table 1 together with the shortest distances between the substituting W (Mo) atom. Notice that below (above) a 50 at% concentration of substituting atoms, we are talking about the Mo_{1-x}W_xS₂ (W_{1-x}Mo_xS₂) alloys. In both cases, the substituting atoms prefer to distribute homogeneously in the host material, forming solid solutions. This is supported by relatively large distances between W (Mo) of about 6.3 Å for concentrations up to 25 at%. At this concentration, we have also obtained the most favorable alloying energies for both Mo_{1-x}W_xS₂ and W_{1-x}Mo_xS₂ alloys (see Figure 2).

Table 1. Calculated lattice parameters a and b (Å) of the 4×4 supercell and dopant closest distances (Å) of the most stable Mo_{1-x}W_xS₂ (or Mo_xW_{1-x}S₂) systems. Experimental data are given in parenthesis [39–41].

Formula	W at%	a, b	W–W	Formula	Mo at%	a, b	Mo–Mo
Mo ₁₆ S ₃₂	0.00	12.683 (12.656)	–	W ₁₆ S ₃₂	0.00	12.642 (12.616)	–
Mo ₁₅ W ₁ S ₃₂	6.25	12.678	–	Mo ₁ W ₁₅ S ₃₂	6.25	12.643	–
Mo ₁₄ W ₂ S ₃₂	12.50	12.675	6.333	Mo ₂ W ₁₄ S ₃₂	12.50	12.646	6.322
Mo ₁₃ W ₃ S ₃₂	18.75	12.672	6.334	Mo ₃ W ₁₃ S ₃₂	18.75	12.648	6.322
Mo ₁₂ W ₄ S ₃₂	25.00	12.669	6.334	Mo ₄ W ₁₂ S ₃₂	25.00	12.651	6.325
Mo ₁₁ W ₅ S ₃₂	31.25	12.667	3.167	Mo ₅ W ₁₁ S ₃₂	31.25	12.652	3.163
Mo ₁₀ W ₆ S ₃₂	37.50	12.664	3.166	Mo ₆ W ₁₀ S ₃₂	37.50	12.655	3.164
Mo ₉ W ₇ S ₃₂	43.75	12.662	3.166	Mo ₇ W ₉ S ₃₂	43.75	12.657	3.164
Mo ₈ W ₈ S ₃₂	50.00	12.659	3.165	Mo ₈ W ₈ S ₃₂	50.00	12.659	3.165

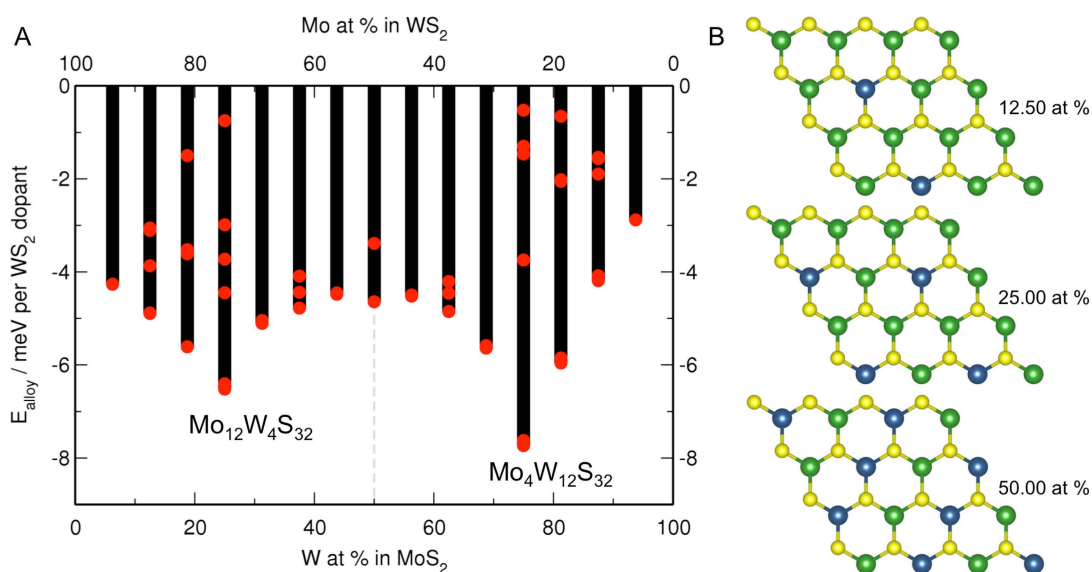


Figure 2. (A) Calculated alloying energies of Mo_{1-x}W_xS₂ systems ($x = 0 - 1$). Numbers calculated according to the Equation (2); (B) Selected alloys with the most stable W arrangement for a given concentration. Green, Mo; blue, W; yellow, S.

It has to be stressed at this point that for larger supercell models, it might be possible to obtain more favorable alloys with larger concentrations of W or Mo. For example, Gan *et al.* [24] and Kutana *et al.* [25] have reported the maximum formation/mixing energies for the W concentrations in the range of 33%–60%. Nevertheless, our trends agree well with other DFT-based works, showing solid solution formation in Mo/W disulfide alloys [24–26].

The lattice parameters of alloy materials are always in between the pure materials and change linearly with the concentration of W (Mo) doping atoms. This is also shown in Figure 3A.

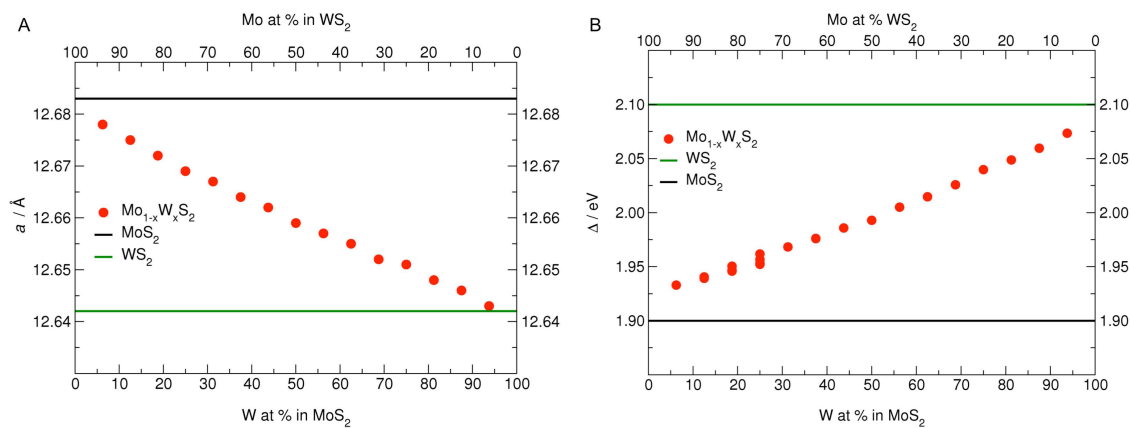


Figure 3. (A) The change of lattice parameter a and (B) the band gap Δ in Mo_{1-x}W_xS₂ systems ($x = 0 - 1$). The values of MoS₂ and WS₂ monolayers are shown with black and green horizontal lines, respectively.

Moreover, the electronic properties are also changed for various alloys (see Figure 3B), namely the band gaps change in a linear manner. Pure MoS₂ and WS₂ monolayers are direct-gap semiconductors with band gaps of 1.84 and 2.01 eV, respectively. These values agree very well with other theoretical and experimental data [1–3,5]. Mo_{1-x}W_xS₂ alloys offer mono-layered materials with band gaps in the range 1.84–2.01 eV. Although the range of available band gaps is not large, the idea of ternary alloys is very interesting in the fields of nanoelectronics, and other TMC alloys, with a more distinct difference in the band gap values, might offer an even larger range of properties.

We have analyzed the electronic structures of W/Mo disulfide alloys in more detail. Figures 4 and 5 show the band structures and density of states of pure materials and the 50%–50% mixture. We have calculated the band structures at two different levels of theory, namely with and without relativistic effects of spin-orbit coupling. TMC materials are well known to exhibit giant spin-orbit splitting, which might of course be altered by alloy formation.

Figure 4 shows that the bands of alloys are exactly in between the bands of pure materials. Furthermore, the density of states shows perfect mixing and hybridization between Mo and W atoms in the alloy. Both metal atoms contribute equally to the states close to the Fermi level. The band edges, valence band maximum (VBM) and conduction band minimum (CBM), in all three materials are situated at the high-symmetry K point, showing that alloy formation does not affect the direct-gap characteristics of TMCs. Therefore, alloys might be interesting for optoelectronic applications.

Figure 5 shows a more detailed electronic band structure of the pure materials and the 50%–50% mixture as extreme cases. MoS₂ and WS₂ exhibit spin-orbit splitting (Δ_{SOC}) in the VBMs of 150 and 425 meV, respectively. These results agree perfectly with other reports available in the literature [12,13]. The alloy materials also exhibit strong Δ_{SOC} , which again is between the values of the pure phases. In the discussed case, we have obtained Δ_{SOC} of 279 meV in the VBM. These results are in agreement with DFT calculations by Wang *et al.* [26], who obtained Δ_{SOC} of 182, 452 and 305 meV for MoS₂, WS₂ and Mo_{0.5}W_{0.5}S₂, respectively, at the LDA level of theory. However, the same authors performed experimental investigations and reported bowing of Δ_{SOC} for different alloys, rather than a linear trend, which has not yet been anticipated by theory.

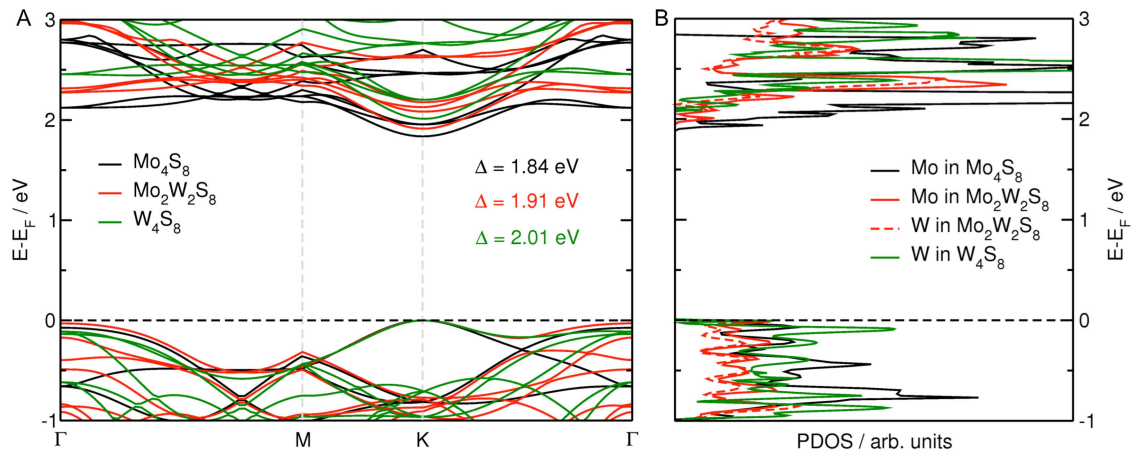


Figure 4. Electronic band structure (A) and density of states (B) of MoS_2 , WS_2 and $\text{Mo}_{0.5}\text{W}_{0.5}\text{S}_2$ systems. The fundamental band gaps are indicated. The projection of states is shown on metal atoms. The Fermi level is shifted to the valence band maximum. No spin-orbit coupling is taken into account.

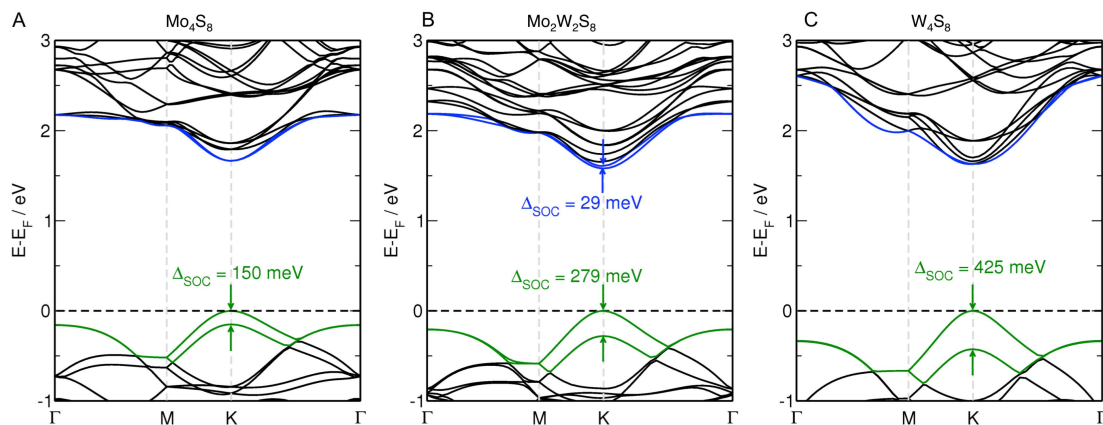


Figure 5. Calculated band structures of MoS_2 , WS_2 and $\text{Mo}_{0.5}\text{W}_{0.5}\text{S}_2$ systems with spin-orbit coupling (Δ_{SOC}).

Moreover, alloys offer extra Δ_{SOC} in the CBM, which reaches about 30 meV for the 50%–50% mixture and which is almost suppressed in the parental monolayers. The spin-splitting in CBM reveals also a small Rashba effect (not discussed here). These features make ternary alloys much more interesting for opto- and spintronic applications compared to pure TMC materials.

We have further analyzed the alloy formation effect on the heat capacity and the Raman normal modes. Selected results are shown in Figure 6. It should be noted that the heat capacity values are lower than the $3R$ (R —gas constant) limit, because they do not include the phonon contribution. Nevertheless, the trends should not be significantly affected. The results show the lowering of the heat capacity of ternary alloys compared to the pure materials, especially at room temperature. This suggests that alloys or small dopings in TMC monolayers might be useful in search for thermoelectric materials. The electronic components of the figure of merit (ZT) for conventional 3D crystals are interrelated in such a way that it is difficult to control them independently to increase ZT . This problem is solved in low-dimensional materials, such as monolayers. Moreover, lowering the heat capacity decreases the thermal conductivity and, as a result, increases ZT .

We have analyzed the normal modes of MoS_2 and alloys of up to a 50 at% W concentration. Phonon calculations in alloys become very complex and are computationally demanding. Our results show that the MoS_2 -like A_{1g} modes (which correspond to the out of plane symmetric vibrations of the S atoms) increase slightly with W concentration. On the other hand, the MoS_2 -like E_{2g} modes

(in-plane symmetric vibrations) decrease with W concentration. At a mixture of 30% (W)–70% (Mo) and larger, the WS_2 -like modes start to appear, resulting in a two-mode behavior for each of the two normal modes. This is in a good agreement with experimental data reported by Liu *et al.* [27].

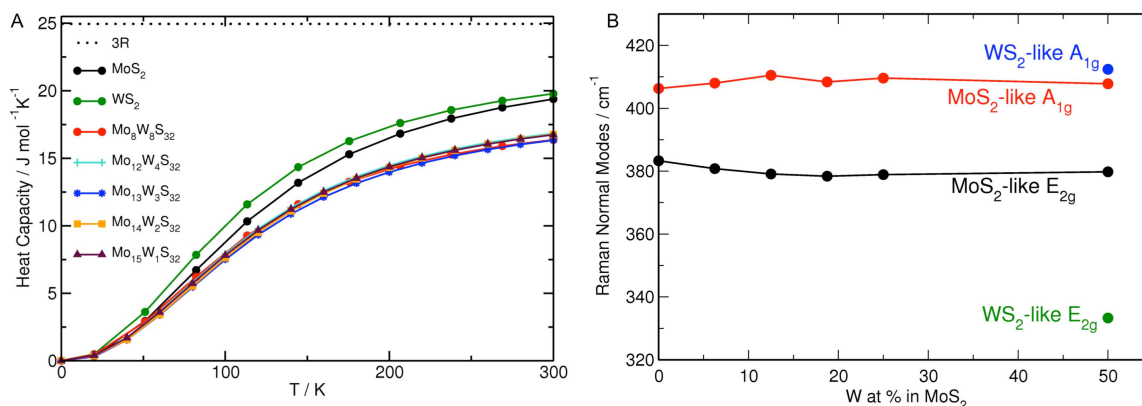


Figure 6. (A) Heat capacity and (B) Raman normal modes change with the W concentration in the MoS_2 monolayer. The normal modes are indicated.

3.2. MoS_2 Alloys with Nb

NbS_2 is a metallic transition-metal dichalcogenide. When alloyed with MoS_2 , even in a very small concentration, it introduces metallic states in the band gap.

The lattice parameters and the smallest Nb – Nb distances of $Mo_{1-x}Nb_xS_2$ systems (with $x = 0$ – 0.25) are shown in Table 2. The distances between the doping/alloying metal atoms in the MoS_2 monolayer of only about 3.3 Å suggest phase separation, as this distance corresponds to the first metal neighbors. This is also shown in Figure 7, where the alloying energy is plotted together with the most stable structure of the $Mo_{0.75}Nb_{0.25}S_2$ alloy.

Table 2. Calculated lattice parameters a and b (Å) of the 4×4 supercell and dopant closest distances (Å) of the most stable $Mo_{1-x}Nb_xS_2$ systems. Experimental data are given in parenthesis [39–41].

Formula	Nb at%	a, b	Nb–Nb
$Mo_{16}S_{32}$	0.00	12.683 (12.656)	–
$Mo_{15}Nb_1S_{32}$	6.25	12.678	–
$Mo_{14}Nb_2S_{32}$	12.50	12.675	3.325
$Mo_{13}Nb_3S_{32}$	18.75	12.672	3.380
$Mo_{12}Nb_4S_{32}$	25.00	12.669	3.394
$Nb_{16}S_{32}$	100.00	13.348 (13.240)	3.338

The alloying energies are positive, meaning that it is rather unlikely that Nb will easily mix into the matrix of MoS_2 monolayers. These energies, however, become nearly zero for Nb concentration above 15 at%, as at this point, the dopants start to cluster inside the host material. Ivanovskaya *et al.* [17,19] have also reported clustering of Nb atoms in nanotubes and monolayers; however, they obtained negative formation energies from the density functional-based tight-binding (DFTB) calculations.

We have calculated the electronic structure of the $Mo_{0.9375}Nb_{0.0625}S_2$ alloy and compared it to those of pure MoS_2 and NbS_2 materials. To manage the computational complexity, these calculations were performed without spin-orbit correction; however, it should be pointed out that spin-splitting occurs also in the case of metallic NbS_2 . Since we have considered only one Nb atom in the supercell, the calculations are spin-polarized, and both alpha and beta electrons are plotted.

The band structures of atom-projected densities of states are shown in Figure 8. These calculations were performed for the largest supercells considered in this work, in order to show the band structure

change for the smallest Nb concentration in a given model (6.25 at%). The Nb atom has one electron less than the Mo atom in the valence shell; therefore, an introduction of a single Nb results in an electron hole, which acts as an acceptor impurity. Similar results were obtained from DFTB calculations by Ivanovskaya *et al.* [19].

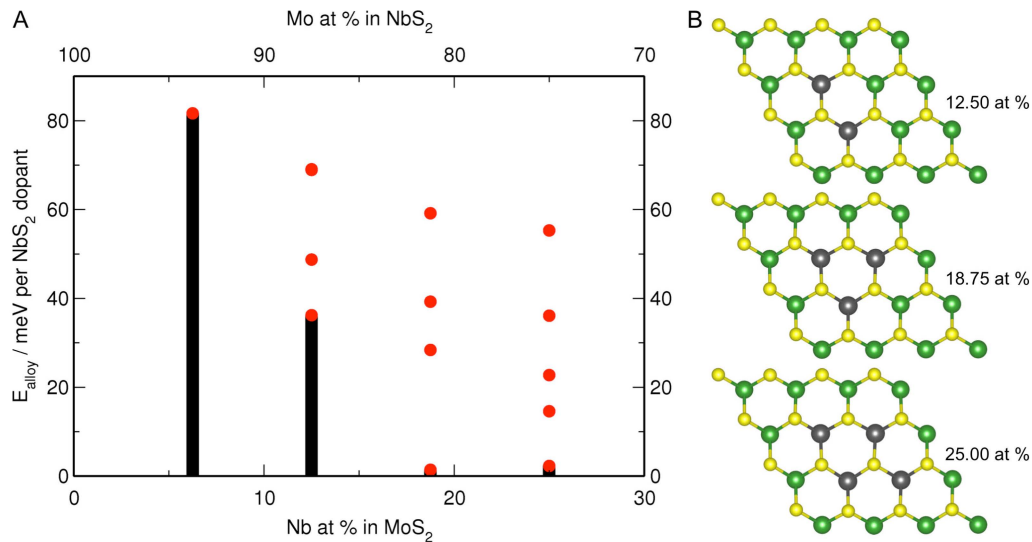


Figure 7. (A) The alloying energies (E_{alloy} , in meV per NbS_2 unit) of the $\text{Mo}_{1-x}\text{Nb}_x\text{S}_2$ systems and (B) selected alloys with the most stable Nb arrangement for a given concentration. Green, Mo; grey, Nb; yellow, S.

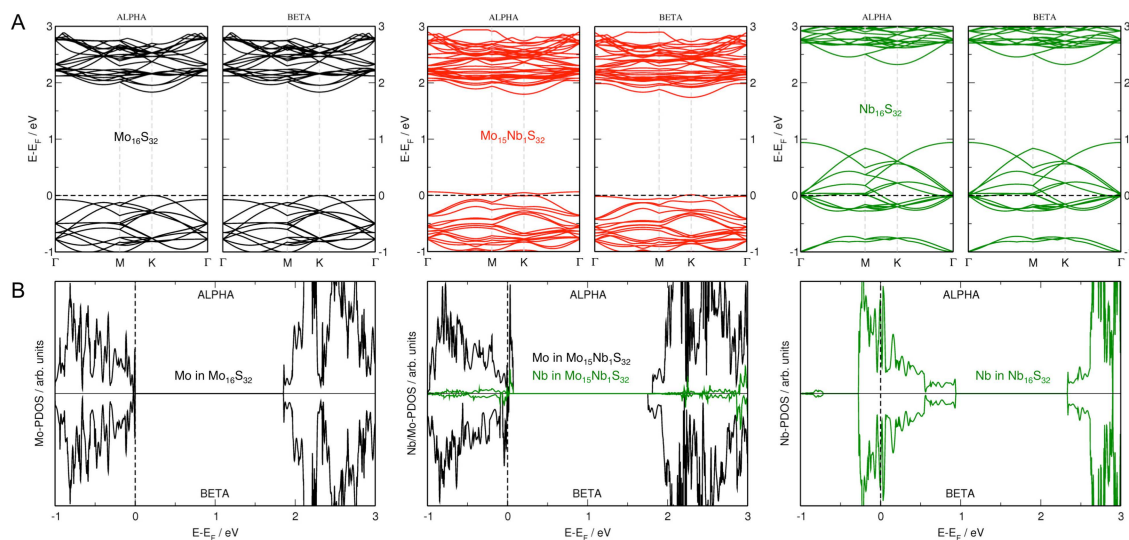


Figure 8. Spin-polarized electronic band structure (A) and density of states (B) of MoS_2 , NbS_2 and $\text{Mo}_{0.9275}\text{Nb}_{0.0625}\text{S}_2$ systems. The projection of states is shown on metal atoms. The Fermi level is indicated by the dashed horizontal line. No spin-orbit coupling is taken into account.

3.3. MoS_2 Alloys with Se

Here, we discuss the substitution of S by Se atoms. In this case, there are several possibilities, as the chalcogen atom may be substituted in only one layer or in both layers. In the latter case, the substitution can be symmetric or asymmetric. Since the substitution is more favorable in two layers, we will show only this case. Moreover, the alloying energies of symmetric and asymmetric alloys are very similar, meaning that polymorphism can be expected. Table 3 shows the lattice parameters and

the shortest Se–Se distances in the symmetric substitution cases, unless otherwise stated. Again, the lattice parameters change in a linear manner with the Se concentration, similar to the W-based alloys. Furthermore, Se atoms distribute homogeneously in the MoS₂ monolayer with the shortest distance of about 5.5 Å up to a 20 at% concentration. This means that Se, similar to W, forms a solid solution with the MoS₂ matrix.

Table 3. Calculated lattice parameters a and b (Å) of the 4×4 supercell, dopant closest distances (Å) and the band gaps, Δ (eV), of the most stable MoSe_{1-x}S_x systems with Se atoms included in both chalcogen layers. Experimental data are given in parenthesis [1,39–42].

Formula	MoSe ₂ at%	a, b	Se–Se	Δ
Mo ₁₆ S ₃₂	0.00	12.683 (12.656)	–	1.90 (1.80)
Mo ₁₆ S ₃₀ Se ₂	6.25	12.710	–	1.81
Mo ₁₆ S ₂₈ Se ₄	12.50	12.738	5.520	1.79
Mo ₁₆ S ₂₆ Se ₆	18.75	12.767	5.532	1.77
Mo ₁₆ S ₂₄ Se ₈	25.00	12.795	5.540	1.75
Mo ₁₆ S ₁₆ Se ₁₆	50.00 symmetric	12.915	3.246	1.63
Mo ₁₆ S ₁₆ Se ₁₆	50.00 asymmetric	12.903	3.243	1.68
Mo ₁₆ Se ₃₂	100.00	13.261 (13.152)	3.288	1.53 (1.55)

The mixing of Se into MoS₂ is energetically very favorable (see Figure 9) for any concentration of at least up to 25 at%. Various distributions of Se are in principle possible, as alloying energies of different systems are very close in value. Moreover, the energies are one order of magnitude larger than in the case of W-alloys, which means that mixing of MoS₂ with MoSe₂ is even more probable. However, we have obtained somewhat lower formation energies than reported by Kang *et al.* [43]. This might be due to the relation of formation energies to the number of atoms: we are referring to the number of MoSe₂ units inside the MoS₂, while Kang *et al.* refer to the number of anions.

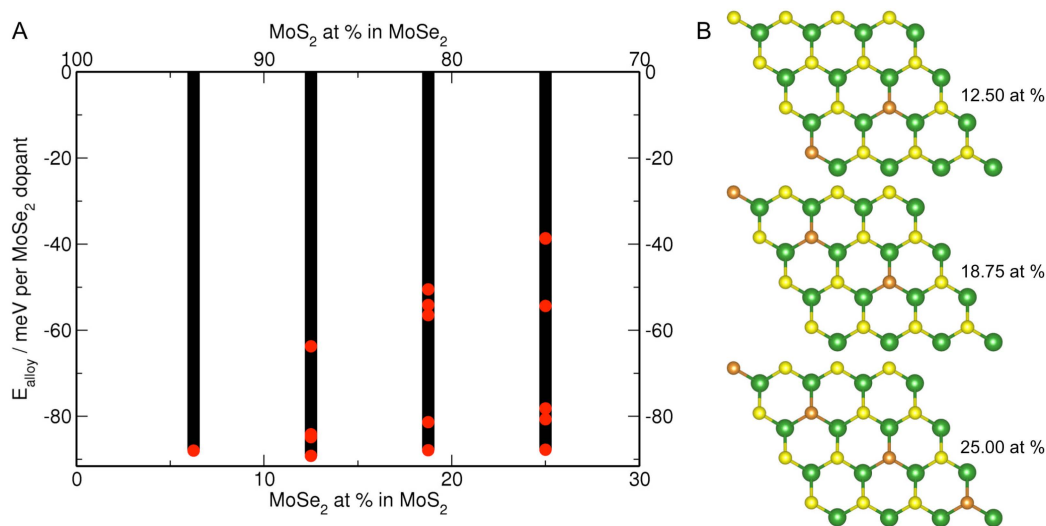


Figure 9. (A) The alloying energies (E_{alloy} , in meV per MoSe₂ unit) of the MoSe_{1-x}S_x systems with Se atoms included in both chalcogen layers and (B) selected alloys with the most stable symmetric Se arrangement for a given concentration. Green, Mo; orange, Se; yellow, S.

For the Se-based alloys, we have again calculated the electronic band structures with and without spin-orbit corrections. Figure 10 shows the electronic band structure and atom-projected densities of states calculated without spin-orbit coupling. The 50%–50% symmetric alloy is a direct-band gap semiconductor, similar to the pure materials, with a band gap of 1.63 eV just in between MoS₂ (1.84 eV)

and MoSe₂ (1.53 eV). In the case of Se-based MoS₂ alloys, we can tune the band gap in the range of about 300 meV, which is already larger than for the case of W-based systems (about 150 meV).

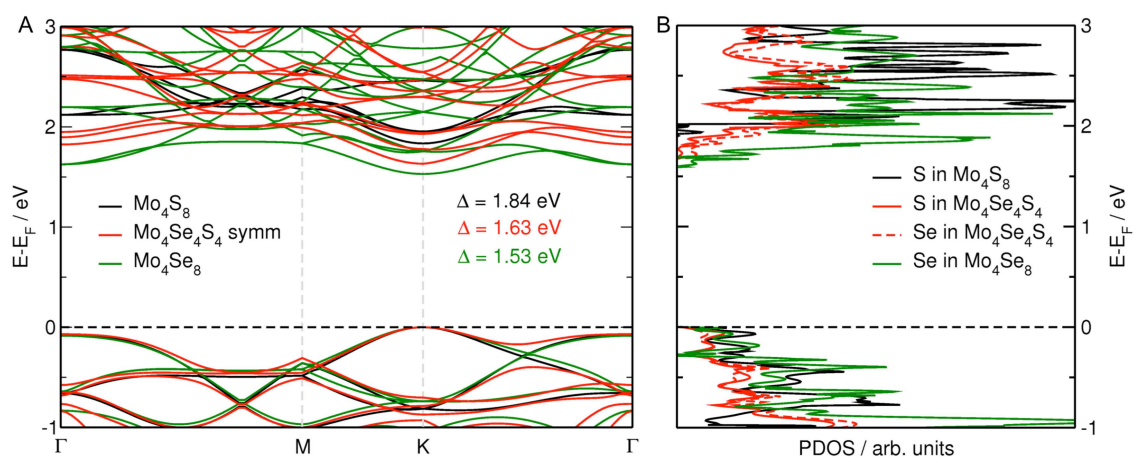


Figure 10. Electronic band structure (A) and density of states (B) of MoS₂, MoSe₂ and MoSeS systems. The fundamental band gaps are indicated. The projection of states is shown on chalcogen atoms. The Fermi level is shifted to the valence band maximum. No spin-orbit coupling is taken into account.

The projected density of states shows that once again, the doping atoms are well incorporated into the host materials, with both S and Se atoms contributing equally to the states close to the Fermi level.

The spin-orbit corrected calculations show that also Se-based alloys exhibit large spin-orbit splitting of about 170–180 meV in the case of a 50%–50% mixture (see Figure 11). These values are just in between those of the pure MoS₂ (150 meV) and MoSe₂ (192 meV) materials.

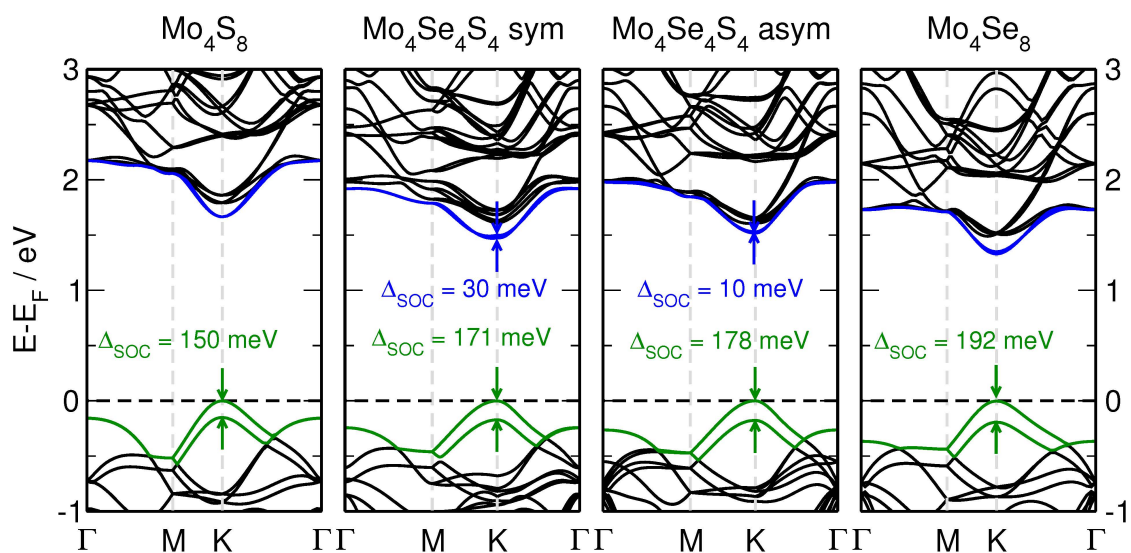


Figure 11. Calculated band structures of MoS₂, MoSe₂, and MoSeS systems with spin-orbit coupling (Δ_{SOC}).

The above results show that the MoS₂-based alloys with W and Se are very good candidates for various applications, including optoelectronics, spintronics or even thermoelectrics. The electronic properties can be tuned in a controlled manner with any features that are in between those of the pure systems, which form the alloys. This means that carefully choosing the systems, with given band gaps or given spin-orbit splitting, will result in very promising alloys. These conclusions and predictions might not only be limited to monolayers, but could as well open a field for bi- and multi-layered alloys.

4. Conclusions

We have studied ternary alloys of the MoS₂ monolayer with W, Nb and Se atoms from first-principles. Our results show that W and Se incorporate easily into the host material and distribute homogeneously, resulting in a solid solution. On the other hand, Nb atoms cluster together for larger metal concentrations and form phase separation. Energetically, the Nb alloys are not very favorable for smaller concentrations, while W and Se easily form mixture materials with MoS₂.

All studied materials show, however, significant changes in the electronic structures compared to the pure parental MoS₂ monolayer. Especially in the case of Nb atoms, the semiconducting MoS₂ shows first localized metallic states for a small metal concentration and, later, full metallic bands for a larger amount of Nb. In the cases of W and Se alloys, the band structures change in such a way that the electronic properties are somewhere in between the intrinsic properties of the pure materials. For example, the spin-splitting of the valence band in MoS₂ and WS₂ is calculated to be 150 meV and 425 meV, respectively, while the 50% mixture exhibits 279 meV. Moreover, spin-splitting occurs in the conduction band with the value of about 30 meV for the Mo_{0.5}W_{0.5}S₂. Furthermore, the optical/fundamental band gaps of the semiconducting alloys are direct gaps with values in between the pure phases, e.g., the band gaps of MoS₂, MoSe₂ and MoSeS are 1.84 eV, 1.63 eV and 1.53 eV, respectively.

Alloys allow tuning of the optical and spintronic properties of transition-metal dichalcogenide materials in a wide range. This feature could be further exploited in the bi- and multi-layered materials, which would probably result in even more interesting properties.

Acknowledgments: The European Commission (FP7-PEOPLE-2012-ITN MoWSeS, GA 317451).

Author Contributions: Agnieszka Kuc and Thomas Heine generated, analyzed and discussed the results. Both authors contributed to writing this paper.

Conflicts of Interest: The authors declare no conflict of interest.

References

1. Mak, K.F.; Lee, C.; Hone, J.; Shan, J.; Heinz, T.F. Atomically Thin MoS₂: A New Direct-Gap Semiconductor. *Phys. Rev. Lett.* **2010**, *105*, 136805. [[CrossRef](#)] [[PubMed](#)]
2. Splendiani, A.; Sun, L.; Zhang, Y.B.; Li, T.S.; Kim, J.; Chim, C.Y.; Galli, G.; Wang, F. Emerging Photoluminescence in Monolayer MoS₂. *Nano Lett.* **2010**, *10*, 1271–1275. [[CrossRef](#)] [[PubMed](#)]
3. Kuc, A.; Zibouche, N.; Heine, T. Influence of quantum confinement on the electronic structure of the transition metal sulfide TS₂. *Phys. Rev. B* **2011**, *83*, 245213. [[CrossRef](#)]
4. Komsa, H.-P.; Krasheninnikov, A.V. Two-Dimensional Transition Metal Dichalcogenide Alloys: Stability and Electronic Properties. *J. Phys. Chem. Lett.* **2012**, *3*, 3652–3656. [[CrossRef](#)] [[PubMed](#)]
5. Ataca, C.; Sahin, H.; Ciraci, S. Stable, Single-Layer MX₂ Transition-Metal Oxides and Dichalcogenides in a Honeycomb-Like Structure. *J. Phys. Chem. C* **2012**, *116*, 8983–8999. [[CrossRef](#)]
6. Zibouche, N.; Philipsen, P.; Kuc, A.; Heine, T. Transition-metal dichalcogenide bilayers: Switching materials for spintronic and valleytronic applications. *Phys. Rev. B* **2014**, *90*, 125440. [[CrossRef](#)]
7. Ramasubramaniam, A.; Naveh, D.; Towe, E. Tunable band gaps in bilayer transition-metal dichalcogenides. *Phys. Rev. B* **2011**, *84*, 205325. [[CrossRef](#)]
8. Ghorbani-Asl, M.; Zibouche, N.; Wahiduzzaman, M.; Oliveira, A.F.; Kuc, A.; Heine, T. Electromechanics in MoS₂ and WS₂: Nanotubes vs. monolayers. *Sci. Rep.* **2013**, *3*, 2961. [[CrossRef](#)] [[PubMed](#)]
9. Johari, P.; Shenoy, V.B. Tuning the Electronic Properties of Semiconducting Transition Metal Dichalcogenides by Applying Mechanical Strains. *ACS Nano* **2012**, *6*, 5449–5456. [[CrossRef](#)] [[PubMed](#)]
10. Yue, Q.; Kang, J.; Shao, Z.; Zhang, X.; Chang, S.; Wang, G.; Qin, S.; Li, J. Mechanical and electronic properties of monolayer MoS₂ under elastic strain. *Phys. Lett. A* **2012**, *376*, 1166–1170. [[CrossRef](#)]
11. Yun, W.S.; Han, S.W.; Hong, S.C.; Kim, I.G.; Lee, J.D. Thickness and strain effects on electronic structures of transition metal dichalcogenides: 2H-MX₂ semiconductors (M = Mo, W; X = S, Se, Te). *Phys. Rev. B* **2012**, *85*, 033305. [[CrossRef](#)]

12. Zhu, Z.Y.; Cheng, Y.C.; Schwingenschlögl, U. Giant spin-orbit-induced spin splitting in two-dimensional transition-metal dichalcogenide semiconductors. *Phys. Rev. B* **2011**, *84*, 153402. [[CrossRef](#)]
13. Zibouche, N.; Kuc, A.; Musfeldt, J.; Heine, T. Transition-metal dichalcogenides for spintronic applications. *Ann. der Phys.* **2014**, *526*, 395–401. [[CrossRef](#)]
14. Nayak, A.P.; Bhattacharyya, S.; Zhu, J.; Liu, J.; Wu, X.; Pandey, T.; Jin, C.; Singh, A.K.; Akinwande, D.; Lin, J.-F. Pressure-induced semiconducting to metallic transition in multilayered molybdenum disulfide. *Nat. Commun.* **2014**, *5*, 3731. [[CrossRef](#)] [[PubMed](#)]
15. Zhao, Z.; Zhang, H.; Yuan, H.; Wang, S.; Lin, Y.; Zeng, Q.; Xu, G.; Liu, Z.; Solanki, G.K.; Patel, K.D.; et al. Pressure induced metallization with absence of structural transition in layered molybdenum diselenide. *Nat. Commun.* **2015**, *6*, 7312. [[CrossRef](#)] [[PubMed](#)]
16. Yadgarov, L.; Rosentsveig, R.; Leitus, G.; Albu-Yaron, A.; Moshkovich, A.; Perfilyev, V.; Vasic, R.; Frenkel, A.I.; Enyashin, A.N.; Seifert, G.; et al. Controlled Doping of MS₂ (M=W, Mo) Nanotubes and Fullerene-like Nanoparticles. *Angew. Chem. Int. Edit.* **2012**, *51*, 1148–1151. [[CrossRef](#)] [[PubMed](#)]
17. Ivanovskaya, V.V.; Heine, T.; Gemming, S.; Seifert, G. Structure, stability and electronic properties of composite Mo_{1-x}Nb_xS₂ nanotubes. *Phys. Stat. Solidi B* **2006**, *243*, 1757–1764. [[CrossRef](#)]
18. Ivanovskaya, V.V.; Seifert, G.; Ivanovskii, A.L. Electronic structure of niobium-doped molybdenum disulfide nanotubes. *Russ. J. Inorg. Chem.* **2006**, *51*, 320–324. [[CrossRef](#)]
19. Ivanovskaya, V.V.; Zobelli, A.; Gloter, A.; Brun, N.; Serin, V.; Colliex, C. *Ab initio* study of bilateral doping within the MoS₂-NbS₂ system. *Phys. Rev. B* **2008**, *78*, 134104. [[CrossRef](#)]
20. Tan, C.-K.; Tansu, N. Auger recombination rates in dilute-As GaNAs semiconductor. *AIP Adv.* **2015**, *5*, 057135. [[CrossRef](#)]
21. Kimura, A.; Paulson, C.A.; Tang, H.F.; Kuech, T.F. Epitaxial GaN_{1-y}As_y layers with high As content grown by metalorganic vapor phase epitaxy and their band gap energy. *Appl. Phys. Lett.* **2004**, *84*, 1489–1491. [[CrossRef](#)]
22. Tansu, N.; Yeh, J.-Y.; Mawst, L. High-Performance 1200-nm InGaAs and 1300-nm InGaAsN Quantum Well Lasers by Metalorganic Chemical Vapor Deposition. *Sel. Top. Quantum Electron. IEEE* **2003**, *9*, 1220–1227. [[CrossRef](#)]
23. Bank, S.; Goddard, L.; Wistey, M.A.; Yuen, H.B.; Harris, J.S. On the temperature sensitivity of 1.5- μ m GaInNAsSb lasers. *Sel. Top. Quantum Electron. IEEE* **2005**, *11*, 1089–1098. [[CrossRef](#)]
24. Gan, L.-Y.; Zhang, Q.; Zhao, Y.-J.; Cheng, Y.; Schwingenschlögl, U. Order-disorder phase transitions in the two-dimensional semiconducting transition metal dichalcogenide alloys Mo_{1-x}W_xX₂ (X = S, Se, and Te). *Sci. Rep.* **2014**, *4*, 6691. [[CrossRef](#)] [[PubMed](#)]
25. Kutana, A.; Penev, E.S.; Yakobson, B.I. Engineering electronic properties of layered transition-metal dichalcogenide compounds through alloying. *Nanoscale* **2014**, *6*, 5820–5825. [[CrossRef](#)] [[PubMed](#)]
26. Wang, G.; Robert, C.; Suslu, A.; Chen, B.; Yang, S.; Alamdari, S.; Gerber, I.C.; Amand, T.; Marie, X.; Tongay, S.; et al. Spin-orbit engineering in transition metal dichalcogenide alloy monolayers. *Nat. Commun.* **2015**. [[CrossRef](#)] [[PubMed](#)]
27. Liu, H.; Antwi, K.K.A.; Chua, S.; Chi, D. Vapor-phase growth and characterization of Mo_{1-x}W_xS₂ (0 \leq x \leq 1) atomic layers on 2-inch sapphire substrates. *Nanoscale* **2014**, *6*, 624–629. [[CrossRef](#)] [[PubMed](#)]
28. Chen, Y.; Dumcenco, D.O.; Zhu, Y.; Zhang, X.; Mao, N.; Feng, Q.; Zhang, M.; Zhang, J.; Tan, P.-H.; Huang, Y.-S.; et al. Composition-dependent Raman modes of Mo_{1-x}W_xS₂ monolayer alloys. *Nanoscale* **2014**, *6*, 2833–2839. [[CrossRef](#)] [[PubMed](#)]
29. Ren, X.; Ma, Q.; Fan, H.; Pang, L.; Zhang, Y.; Yao, Y.; Ren, X.; Liu, S.F. A Se-doped MoS₂ nanosheet for improved hydrogen evolution reaction. *Chem. Commun.* **2015**, *51*, 15997–16000. [[CrossRef](#)] [[PubMed](#)]
30. Faraji, M.; Sabzali, M.; Yousefzadeh, S.; Sarikhani, N.; Ziashahabi, A.; Zirak, M.; Moshfegh, A.Z. Band engineering and charge separation in the Mo_{1-x}W_xS₂/TiO₂ heterostructure by alloying: First principle prediction. *RSC Adv.* **2015**, *5*, 28460–28466. [[CrossRef](#)]
31. Dovesi, R.; Saunders, V.R.; Roetti, R.; Orlando, R.; Zicovich-Wilson, C.M.; Pascale, F.; Civalieri, B.; Doll, K.; Harrison, N.M.; Bush, I.J.; et al. *CRYSTAL09 User's Manual*; University of Torino: Torino, Canada, 2009.
32. Perdew, J.P.; Burke, K.; Ernzerhof, M. Generalized Gradient Approximation Made Simple. *Phys. Rev. Lett.* **1996**, *77*, 3865. [[CrossRef](#)] [[PubMed](#)]
33. Cora, F.; Patel, A.; Harrison, N.M.; Roetti, C.; Catlow, C.R.A. An ab-initio Hartree-Fock study of alpha-MoO₃. *J. Mater. Chem.* **1997**, *7*, 959. [[CrossRef](#)]

34. Cora, F.; Patel, A.; Harrison, N.M.; Dovesi, R.; Catlow, C.R.A. An ab-initio Hartree-Fock study of the cubic and tetragonal phases of Bulk Tungsten Trioxide. *J. Am. Chem. Soc.* **1996**, *118*, 12174. [[CrossRef](#)]
35. Dall'Olio, S.; Dovesi, R.; Resta, R. Spontaneous polarization as a Berry phase of the Hartree-Fock wave function: The case of KNbO₃. *Phys. Rev. B* **1997**, *56*, 10105–10114. [[CrossRef](#)]
36. Te Velde, G.; Baerends, E. J. Precise density-functional method for periodic structures. *Phys. Rev. B* **1991**, *44*, 7888–7903. [[CrossRef](#)]
37. Philipsen, P.; te Velde, G.; Baerends, E.; Berger, J.; de Boeij, P.; Groenveld, J.; Kadantsev, E.; Klooster, R.; Kootstra, F.; Romaniello, P.; et al. *BAND2012, SCM, Theoretical Chemistry*; Vrije Universiteit: Amsterdam, Netherlands, 2012.
38. Monkhorst, H.J.; Pack, J.D. Special points for Brillouin-zone integrations. *Phys. Rev. B* **1976**, *13*, 5188. [[CrossRef](#)]
39. Wilson, J.A.; Yoffe, A.D. The transition metal dichalcogenides discussion and interpretation of the observed optical, electrical and structural properties. *Adv. Phys.* **1969**, *18*, 193–335. [[CrossRef](#)]
40. Mattheis, L.F. Band Structures of Transition-Metal-Dichalcogenide Layer Compounds. *Phys. Rev. B* **1973**, *8*, 3719. [[CrossRef](#)]
41. Coehoorn, R.; Haas, C.; Dijkstra, J.; Flipse, C.J.F.; Degroot, R.A.; Wold, A. Electronic structure of MoSe₂, MoS₂, and WSe₂. I. Band-structure calculations and photoelectron spectroscopy. *Phys. Rev. B* **1987**, *35*, 6195–6202. [[CrossRef](#)]
42. Tongay, S.; Zhou, J.; Ataca, C.; Lo, K.; Matthews, T.S.; Li, J.; Grossman, J.C.; Wu, J. Thermally Driven Crossover from Indirect toward Direct Bandgap in 2D Semiconductors: MoSe₂ versus MoS₂. *Nano Lett.* **2012**, *12*, 5576–5580. [[CrossRef](#)] [[PubMed](#)]
43. Kang, J.; Tongay, S.; Li, J.; Wu, J. Monolayer semiconducting transition metal dichalcogenide alloys: Stability and band bowing. *J. Appl. Phys.* **2013**, *113*, 143703. [[CrossRef](#)]



© 2015 by the authors; licensee MDPI, Basel, Switzerland. This article is an open access article distributed under the terms and conditions of the Creative Commons by Attribution (CC-BY) license (<http://creativecommons.org/licenses/by/4.0/>).